

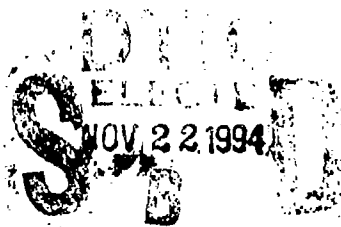
11

AD-A286 421



Derivation of a Wavenumber Filter Design for the Measurement of Turbulent Wall Pressure Fluctuations

William L. Keith
Bruce M. Abraham
Submarine Sonar Department



22 94-35902



Naval Undersea Warfare Center Division
Newport, Rhode Island

94 100 075

PREFACE

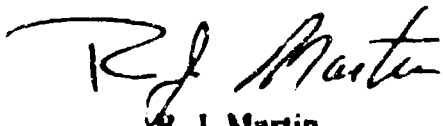
This report was prepared under the NUWC Detachment New London Project entitled *New London Water Tunnel Research*, principal investigator W. L. Keith (Code 2141). It was funded by Code 10 under NUWC Division Newport Job Order No 710B46.

The technical reviewer for this report was T. C. Chen (Code 2141).

A portion of this research was presented at the ASME 1994 Winter Annual Meeting, Symposium on Application of Micro-fabrication to Fluid Mechanics, Chicago, Illinois, 6-11 November 1994.

The authors are grateful for the continued support of Dr K. M. Lima (Code 102).

Reviewed and Approved: 14 November 1994


R. J. Martin
Acting Head, Submarine Sonar Department

REPORT DOCUMENTATION PAGE

Form Approved
OMB No. 0704-0188

Public reporting burden for this collection of information is estimated to average 1 hour per response, including the time for reviewing instructions, searching existing data sources, gathering and maintaining the data needed, and completing and reviewing the collection of information. Send comments regarding this burden estimate or any other aspect of this collection of information, including suggestions for reducing the burden, to Washington Headquarters Services, Directorate for Information Operations and Reports, 1215 Jefferson Davis Highway, Suite 1204, Arlington, VA 22202-4302, and to the Office of Management and Budget, Paperwork Reduction Project (0704-0188), Washington, DC 20503.

1 AGENCY USE ONLY (Leave Blank)			2 REPORT DATE	3 REPORT TYPE AND DATES COVERED	
			14 November 1994	Final	
4 TITLE AND SUBTITLE			5 FUNDING NUMBERS		
Derivation of a Wavenumber Filter Design for the Measurement of Turbulent Wall Pressure Fluctuations					
6 AUTHOR(S)					
William L. Keith and Bruce M. Abraham					
7 PERFORMING ORGANIZATION NAME(S) AND ADDRESS(ES)			8 PERFORMING ORGANIZATION REPORT NUMBER		
Naval Undersea Warfare Center Detachment New London New London Connecticut 06320			TR 10,693		
9 SPONSORING/MONITORING AGENCY NAME(S) AND ADDRESS(ES)			10 SPONSORING/MONITORING AGENCY REPORT NUMBER		
11 SUPPLEMENTARY NOTES					
12a DISTRIBUTION AVAILABILITY STATEMENT			12b DISTRIBUTION CODE		
Approved for public release, distribution is unlimited.					
13 ABSTRACT (Maximum 200 words)					
<p>Measurement of the wavenumber-frequency spectrum $\Phi(k_1, \omega)$ of turbulent wall pressure fluctuations requires a line array (wavenumber filter) of closely spaced sensors. However, the wide range of wavenumbers of the wall pressure fluctuations that contribute to the spectrum imposes constraints on sensor size, spacing, and number. In this study, the Corcos model of the wall pressure field is used in conjunction with recent experimental measurements to determine design parameters expressed in terms of boundary layer length and time scales. For the case of turbulent boundary layers at moderate to high Reynolds numbers, the resulting wavenumber filter design requires micromachining technology.</p>					
14 SUBJECT TERMS			15. NUMBER OF PAGES		
Boundary Layer Filter Design Line Array, Micromachining, Pressure Sensor Turbulent Wall Pressure Field, Wavenumber-Frequency Spectrum			36		
16. PRICE CODE					
17. SECURITY CLASSIFICATION OF THIS REPORT		18. SECURITY CLASSIFICATION OF THIS PAGE	19. SECURITY CLASSIFICATION OF ABSTRACT	20. LIMITATION OF ABSTRACT	
UNCLASSIFIED		UNCLASSIFIED	UNCLASSIFIED	SAR	

TABLE OF CONTENTS

	Page
LIST OF ILLUSTRATIONS	ii
LIST OF TABLES	ii
LIST OF SYMBOLS	iii
INTRODUCTION	1
THE EFFECT OF SENSOR SIZE ON THE WALL PRESSURE FREQUENCY SPECTRUM	2
DERIVATION OF A WAVENUMBER FILTER DESIGN FOR MEASUREMENTS AT HIGH FREQUENCY	3
MEASUREMENTS AT LOW FREQUENCIES	17
DIMENSIONAL WAVENUMBER FILTER PARAMETERS FOR TURBULENT BOUNDARY LAYERS IN AIR AND WATER	20
CONCLUSIONS AND RECOMMENDATIONS	20
REFERENCES.....	23
APPENDIX—SENSOR SIDE EFFECTS ON MEASURED FREQUENCY SPECTRA	A-1

Accession For	
MLW - GRAMI	<input checked="" type="checkbox"/>
DTIC Tech	<input type="checkbox"/>
Unannounced	<input type="checkbox"/>
Justification	
By _____	
Distribution _____	
Availability Desired	
Dist	Avail and/or Recd
A-1	

LIST OF ILLUSTRATIONS

Figure		Page
1	Dimensional Wavenumber-Frequency Spectra at High and Low Frequencies Estimated From the Cross-Spectral Measurements of Keith and Barclay (1993)	5
2	The Corcos Model of the Nondimensional Wavenumber-Frequency Spectrum at Low and High Frequencies	7
3	Wavenumber Filter Details	10
4	Signal Processing Flow Chart	11
5	Spectral Attenuation at the High Frequency Due to the Spanwise or Streamwise Sensor Length	13
6	The Product of the Spanwise Sensor Response (for $0 \leq L_2^* \leq 100$) and the True Spectrum for the High-Frequency Case	13
7	The Product of the Streamwise Sensor Response (for $0 \leq L_1^* \leq 100$) and the True Spectrum for the High-Frequency Case	14
8	The Wavenumber Filter Responses Compared With the True Spectrum for the High-Frequency Case	16
9	Comparison of the Measured Spectrum (for Three Different Wavenumber Filters) With the True Spectrum at the High Frequency	16
10	Nondimensional Wavenumber-Frequency Spectrum for the High- and Low-Frequency Cases From the Corcos Model	18
11	Spectral Attenuation at the Low Frequency Due to the Spanwise or Streamwise Sensor Length	18
12	Comparison of the Measured Spectrum (for Three Different Wavenumber Filters) With the True Spectrum at the Low Frequency	19

LIST OF TABLES

Table		Page
1	Dimensional Wavenumber Filter Parameters for Measurements at High Frequencies in Selected Turbulent Boundary Layers	5

LIST OF SYMBOLS

k_1, k_2	Streamwise, Spanwise Wavenumber (rad/m)
$k_c = \omega/U_c$	Convective Wavenumber (rad/m)
N	Number of Pressure Sensors
$p(x_1, x_2, t)$	Fluctuating Wall Pressure (μPa)
$R_\theta = U_0 \theta / \nu$	Momentum Thickness Reynolds Number
Δx	Streamwise Sensor Spacing (m)
$u_\tau = (\tau/\rho)^{1/2}$	Friction Velocity (m/sec)
δ	Boundary Layer Thickness (m)
ρ	Fluid Density (kg/m^3)
τ	Mean Wall Shear Stress (μPa)
ν	Fluid Kinematic Viscosity (m^2/sec)
$\Phi(\omega)$	Frequency Spectrum ($\mu\text{Pa}^2/(\text{rad/sec})$)
$\Phi(\xi, \eta, \omega)$	Cross Spectrum ($\mu\text{Pa}^2/(\text{rad/sec})$)
$\Phi(k_1, k_2, \omega)$	Wavenumber-Frequency Spectrum ($\mu\text{Pa}^2/(\text{rad}^3/\text{sec}\cdot\text{m}^2)$)
	Magnitude of a Real or Complex Quantity.

DERIVATION OF A WAVENUMBER FILTER DESIGN FOR THE MEASUREMENT OF TURBULENT WALL PRESSURE FLUCTUATIONS

INTRODUCTION

The measurement and analysis of turbulent wall pressure fluctuations are important to problems of flow-induced vibration and noise as well as to studies of turbulence physics. The space time field $p(x_1, x_2, t)$ and associated three-dimensional wavenumber-frequency spectrum $\Phi(k_1, k_2, \omega)$ are of primary interest. To date, they have rarely been directly measured in laboratories due to the extensive number of sensors and signal processing required. A common approach used recently by Karangelen et al. (1991) and Keith and Barclay (1993) has been to estimate the wavenumber-frequency spectrum from cross-spectral measurements made with a small number of sensors at unequal spacings. Although this approach has been useful for estimating the convective ridge region, uncertainties arise due to the limited number of spatial separations at which data are obtained. In particular, these uncertainties preclude accurately estimating the lower spectral levels at wavenumbers outside of the convective ridge region.

Many single point experimental measurements of $p(t)$ and the one-dimensional spectrum $\Phi(\omega)$ have appeared in the literature, as reviewed by Keith et al. (1992). Here, we determine a wavenumber filter design for the measurement of the two-dimensional spectrum $\Phi(k_1, \omega)$. Although arrays of sensors are commonly utilized for acoustic measurements, they are generally not implemented in incompressible fluid mechanics experiments. The methodology is also applicable for fluctuating wall shear stress measurements. However, a widely accepted model for the wall shear stress wavenumber-frequency spectrum required in this analysis does not exist at the present time. This is largely due to the lack of published research on correlation or cross-spectral density measurements of the wall shear stress field.

We are primarily concerned with three array parameters: size, spacing, and number of sensors. Following Blake and Chase (1971), Smol'yakov and Tkachenko (1983), Farabee and Geib (1991), and Manoha (1991), we use a linear array of equally spaced sensors. The mechanical and electrical design of the sensors will not be addressed here. Currently, the size of available sensors poses limitations on the design of a wavenumber filter. Here we assume that microfabrication technology will allow a nearly optimum design to be specified at the outset. The design problem then involves estimating the true field to be measured and determining the effect of the above three parameters on the measured field. The sensors are assumed to have a constant frequency response

and uniform sensitivity over the sensing area. We first briefly review past investigations of sensor size effects on the wall pressure frequency spectrum $\Phi(\omega)$.

THE EFFECT OF SENSOR SIZE ON THE WALL PRESSURE FREQUENCY SPECTRUM

The early work of Corcos (1963) showed that an increase in sensor size leads to a more rapid roll-off of the measured frequency spectrum $\Phi(\omega)$ at high frequencies. This effect has been well established and is supported with the comparisons of published measurements of $\Phi(\omega)$ by Keith et al. (1992). Schewe (1983) measured wall pressure spectra with circular sensors of varying diameter and concluded that the diameter $d^+ = du_\tau/v = 19$ was adequate to resolve $\Phi(\omega)$ at the highest energy-containing frequencies in the turbulent field. Schewe did not report measurements for $d^+ < 19$. The comparisons presented by Keith et al. (1992) showed Schewe's spectral levels (for $d^+ = 19$) scaled with inner variables compared well with the numerical simulation of Choi and Moin (1990) (for $d^+ \approx 18$). However, Keith et al. (1992) also showed that the Corcos (1963) correction increased Schewe's spectral levels (for $d^+ = 19$) by 2.5 dB at the highest frequencies measured.

The pressure sensor diameter d^+ required for proper resolution of $\Phi(\omega)$ at all frequencies and Reynolds numbers remains unknown. Schewe's results showed that sensors with $d^+ > 19$ are inadequate. Head and Bandyopadhyay (1981) and Wei and Willmarth (1989) investigated the effect of R_θ on coherent structures in the near-wall region. Wei and Willmarth (1989) concluded that as R_θ increases, the hairpin vortices become smaller with increased vorticity in the cores. This increased stretching of hairpin vortices with increasing R_θ caused a Reynolds number effect on the near-wall ($y^+ = 15$) normal velocity fluctuations that was not accounted for with an inner variable scaling. As the Reynolds number (based upon the free-stream velocity and one-half channel width) increased from 3,000 to 40,000, the outer length scale δ remained constant and the inner length scale v/u_τ decreased by an order of magnitude. Such a Reynolds number effect could cause the required pressure sensor diameter d^+ to decrease by an amount greater than simply the decrease in v/u_τ . An experiment in which R_θ could be varied over a wider range ($1,000 < R_\theta < 100,000$) with pressure sensors of varying diameter is required to establish this effect. Current sensor technology is inadequate for providing sufficiently small sensors for such an investigation.

DERIVATION OF A WAVENUMBER FILTER DESIGN FOR MEASUREMENTS AT HIGH FREQUENCIES

In order to design a wavenumber filter, we require a model of the true wall pressure field. Although we wish to measure the two dimensional spectrum $\Phi(k_1, \omega)$, we must use a model for the three-dimensional spectrum $\Phi(k_1, k_2, \omega)$ in order to account for the two-dimensional spatial response of the sensors. The Corcos (1963) model of the cross-spectrum of the wall pressure field is given as

$$\Phi(\xi, \eta, \omega) = \Phi(\omega) A(\omega\xi/U_c) e^{-i(\omega\xi/U_c)} B(\omega\eta/U_c), \quad (1)$$

where ξ and η are the streamwise and spanwise separation variables, respectively. Experimental data support exponential forms for $A(\omega\xi/U_c)$ and $B(\omega\eta/U_c)$ given by

$$A(\omega\xi/U_c) = e^{\alpha|\omega\xi/U_c|}, \quad B(\omega\eta/U_c) = e^{\beta|\omega\eta/U_c|}. \quad (2)$$

Farabee and Casarella (1991) noted that the streamwise decay constant α reported from various investigations varies from -0.10 to -0.19, and is a function of various flow parameters. A value for α of -0.125 fits the recent data of Farabee and Casarella (1991) and also Keith and Barclay (1993) at the higher frequencies. A constant of -0.125 implies that a 90-percent reduction in $A(\omega\xi/U_c)$ occurs due to the spatial decay of coherent structures as they convect over three wavelengths in the streamwise direction. At lower values of $\omega\xi/U_c$, the similarity scaling breaks down, as shown by Farabee and Casarella (1991) and Keith and Barclay (1993). The convective wavenumbers in this range exhibit a rapid loss of spatial coherence and lower convection velocities. The similarity scaling is therefore only valid over a limited range of convective wavenumbers and related frequencies. Following Willmarth and Roos (1965), the spanwise decay constant is taken as $\beta = -0.7$.

The wavenumber-frequency spectrum $\Phi(k_1, k_2, \omega_0)$ is defined as

$$\Phi(k_1, k_2, \omega_0) = 1/4\pi^2 \int_{-\infty}^{\infty} \int_{-\infty}^{\infty} \Phi(\xi, \eta, \omega_0) e^{-i(k_1\xi + k_2\eta)} d\xi d\eta. \quad (3)$$

Using equations (1) and (2), equation (3) was evaluated with the symbolic manipulation program MACSYMA (Rand, 1984) to obtain

$$\Phi(k_1, k_2, \omega_0) = \Phi(\omega_0) F_1(k_1, k_c) F_2(k_2, k_c), \quad (4)$$

where

$$F_1(k_1, k_c) = \{1/2\pi k_c\} \{-2\alpha / (\alpha^2 + (k_1/k_c + 1)^2)\} \\ F_2(k_2, k_c) = \{1/2\pi k_c\} \{-2\beta / (\beta^2 + (k_2/k_c)^2)\}. \quad (5)$$

In transforming $\Phi(\xi, \eta, \omega_0)$, $k_c = \omega_0/U_c$ is taken as constant, and the variation of U_c with ξ is neglected. The Corcos model of the two-dimensional wavenumber-frequency spectrum $\Phi(k_1, \omega_0)$ is then

$$\Phi(k_1, \omega_0) = \int_{-\infty}^{\infty} \Phi(k_1, k_2, \omega_0) dk_2 = \Phi(\omega_0) F_1(k_1, k_c). \quad (6)$$

The model of the wavenumber-frequency spectrum given by equation (6) is shown in dimensional form in figure 1. The low and high frequencies chosen correspond to the recent water tunnel investigation of Keith and Barclay (1993) (see table 1). There, the lowest measurable frequency was determined by the acoustic noise in the facility, and the highest frequency by the electronic noise from the sensor preamplifiers. The cross-spectral measurements of Keith and Barclay (1993) agreed well with the Corcos (1963) model given by equations (1) and (2), with the decay constant $\alpha = -0.125$. The decrease of 53 dB in the convective ridge peak level from the low to the high frequency reflects the 36-dB decrease in the measured values of $\Phi(\omega_0)$, and the 17-dB decrease in the function $F_1(k_1, k_c)$. The spectrum $\Phi(k_1, \omega_0)$ in figure 1 may be viewed as an estimate of a typical spectrum, based upon cross-spectral measurements that could be measured directly with a wavenumber filter. The high-frequency portion of the spectrum will determine the minimum sensor size and spacing requirements due to the high wavenumbers involved. The required length of the wavenumber filter will increase significantly for the low-frequency case in order to resolve the narrower convective ridge.

We first estimate the highest nondimensional frequency at which measurements of $\Phi(k_1, \omega_0)$ are to be made that are valid for any turbulent boundary layer. Farabee and Casarella (1991) concluded that for nondimensional frequencies $\omega v/u_\tau^2 \geq 0.3$, contributions to $\Phi(\omega)$ are from velocity fluctuations in the buffer region, and $\Phi(\omega)$ scales with inner variables. We therefore define $k_1^* = k_1 v/u_\tau$, $k_2^* = k_2 v/u_\tau$, $\omega_0^* = \omega_0 v/u_\tau^2$, $U_c^* = U_c/v/u_\tau$, $k_c^* = \omega_0^*/U_c^* = k_c v/u_\tau$,

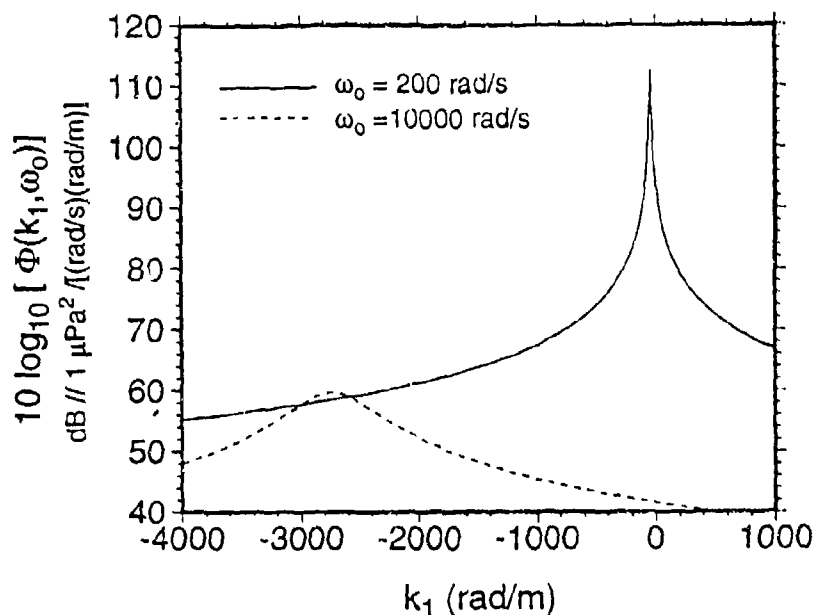


Figure 1. Dimensional Wavenumber-Frequency Spectra at High and Low Frequencies Estimated From the Cross-Spectral Measurements of Keith and Barclay (1993)

Table 1. Dimensional Wavenumber Filter Parameters for Measurements at the High Frequencies in Selected Turbulent Boundary Layers

Investigation	R_θ	U_0 (m/s) (ft/s)	δ (cm) (in)	$5v/u_\tau$ (micron) (in)	$N\Delta x^*$ (cm) (in)	d^+ (used)
Farabee & Casarella (1991) (air)	6.0×10^3	28.3 92.8	2.8 1.1	63.5 2.5×10^{-3}	1.27 .50	66
Willmarth & Wooldridge (1962) (air)	2.9×10^4	47.6 156.0	11.4 4.5	53.3 2.1×10^{-3}	1.07 .42	383
Keith & Barclay (1993) (water)	2.2×10^4	6.1 20.0	3.3 1.3	22.9 9.0×10^{-4}	.46 .18	444
Carey et al. (1967) (water)	7.5×10^4	17.0 55.7	4.3 1.7	9.6 3.8×10^{-4}	.20 .08	915
Undersea Application (sea water)	2.2×10^5	10.3 33.8	21.6 8.5	12.7 5.0×10^{-4}	.25 .10	---

$\Delta x^* = \Delta x u_\tau / v$, and $\Delta t^* = \Delta t u_\tau^2 / v$. The nondimensional frequency spectral levels are then given by $\Phi^*(\omega_0^*) = \Phi(\omega_0)(u_\tau^2/v^2)$ and the wavenumber frequency level is by $\Phi^*(k_1^*, k_2^*, \omega_0^*) = \Phi(k_1, k_2, \omega_0)(u_\tau^2/v^2)(u_\tau/v)^2$. We may express equation (4) in the nondimensional and normalized form as

$$E(k_1^*, k_2^*, \omega_0^*) = \Phi^*(k_1^*, k_2^*, \omega_0^*) / \Phi^*(\omega_0^*) = F_1^*(k_1^*) F_2^*(k_2^*), \quad (7)$$

where

$$\begin{aligned} F_1^*(k_1^*) &= [1/2\pi k_c^*] [-2\alpha/(\alpha^2 + (k_1^*/k_c^* + 1)^2)], \\ F_2^*(k_2^*) &= [1/2\pi k_c^*] [-2\beta/(\beta^2 + (k_2^*/k_c^*)^2)]. \end{aligned} \quad (8)$$

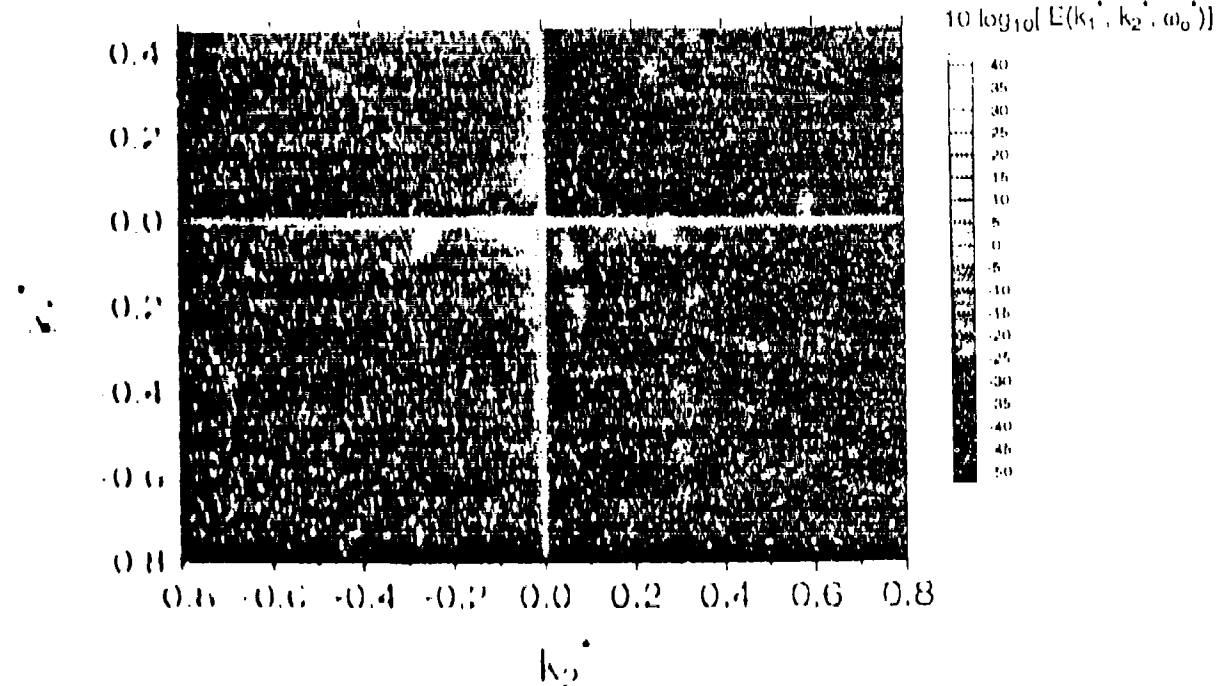
For $E(k_1^*, k_2^*, \omega_0^*)$ as defined above,

$$\int_{-\infty}^{\infty} \int_{-\infty}^{\infty} E(k_1^*, k_2^*, \omega_0^*) dk_1^* dk_2^* = 1. \quad (9)$$

The comparisons of $\Phi^*(\omega_0^*)$ versus ω_0^* given by Keltch et al. (1992) show that for frequencies $\omega_0^* > 3.0$ the spectral levels are at least 40 dB below the highest levels at low frequencies. We therefore define $\omega_0^* = 3.0$ as the highest frequency for which $E(k_1^*, \omega_0^*)$ will be measured. A value for U_c^* is required to determine k_c^* . Experimental measurements of the cross spectrum do not extend to the higher frequencies due to the inherent decay in the spectral levels that occurs with typical finite sensor separations. Convection velocity measurements obtained from the phase of the cross spectrum are therefore also limited to lower frequencies. The highest frequency for which Farabee and Casarella (1991) reported convection velocity measurements was $\omega_0^* = 0.34$ with $U_c^* = 15$. For Choi and Moin's (1990) numerical simulation, the highest frequency was $\omega_0^* = 2.5$ with $U_c^* = 14.3$. We define $U_c^* = 15$ with $k_c^* = 0.2$. The spectrum $E(k_1^*, k_2^*, \omega_0^*)$ evaluated with these parameters is shown in figure 2. The energy is centered at $k_1^* = k_c^* = 0.2$ and at $k_2^* = 0$.

Our wavenumber filter consists of a line array of N rectangular sensors, each having a flat frequency response and uniform spatial sensitivity. The sensors are of nondimensional size, $L_1^* = L_1 u_\tau / v$ by $L_2^* = L_2 u_\tau / v$, and are equally spaced at streamwise increments, Δx^* , as shown in

Low Frequency, $U_0^+ = 15$, $\omega_0^+ = 0.01$



High Frequency, $U_0^+ = 15$, $\omega_0^+ = 3.0$

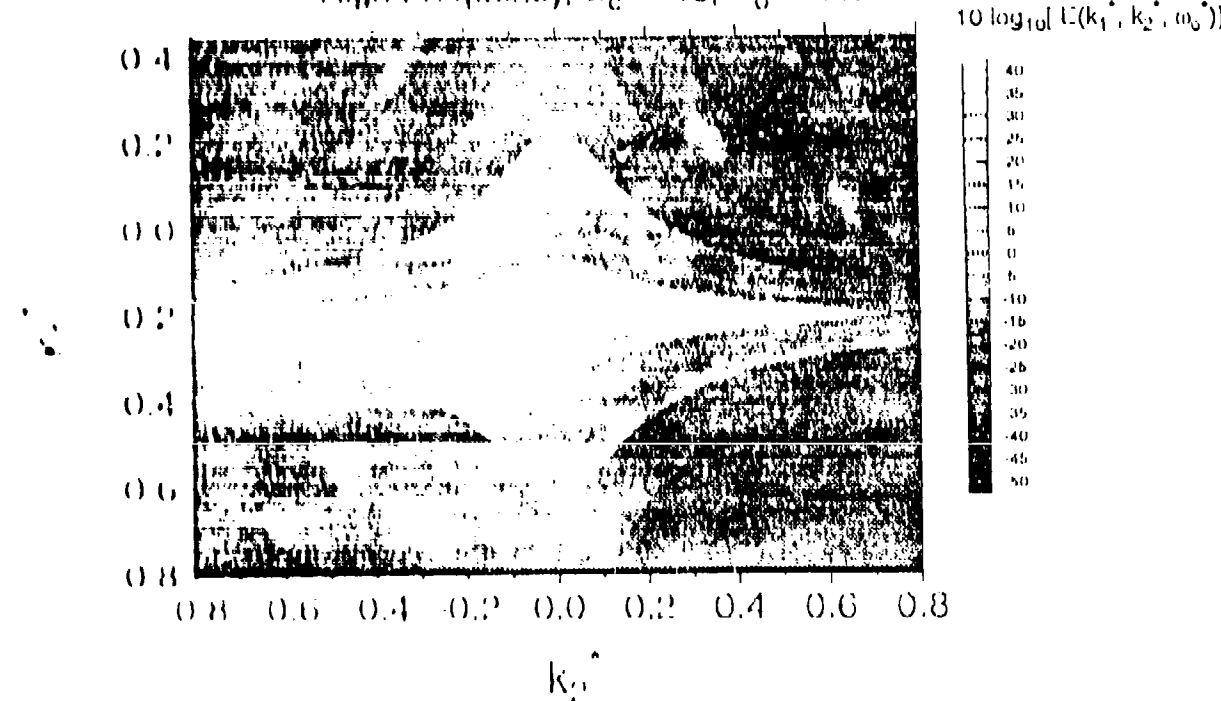


FIGURE 5. The Corcos Model of the Nondimensional Wavenumber Frequency Spectrum
at Low and High Frequencies

figure 3. We have used rectangular rather than circular sensors to simplify the analysis. The sensor voltage outputs $p(n\Delta x^*, t^*)$, $n = 0, 1, 2, \dots, N-1$, are acquired simultaneously in time. The analog data are first bandpass filtered in the time domain. This may be viewed as a two-step process. Unwanted acoustic energy inherent to the flow facility (typically at low frequencies) is removed with frequency filtering. These data are then again filtered at the Nyquist frequency to avoid temporal aliasing. The sensor outputs are next digitized in the time domain to generate $p(n\Delta x^*, m\Delta t^*)$. The discrete temporal Fourier transform of each sensor output is then

$$P_r(n\Delta x^*, \omega_0^*) = \Delta t^*/2\pi \sum_{m=0}^{M-1} w_t(m)p(n\Delta x^*, m\Delta t^*)e^{-i\omega_0^* m\Delta t^*}. \quad (10)$$

Here, $w_t(m)$ is the temporal window, and r refers to the temporal record for the ensemble averaging, $r = 1, 2, \dots, R$. Contemporary analog-to-digital converters and mass storage capabilities allow sufficient sampling, Δt^* , and record length, M , to minimize errors in $P_r(n\Delta x^*, \omega_0^*)$. The discrete spatial Fourier transform of $P_r(n\Delta x^*, \omega_0^*)$ is then

$$H_r(k_1^*, \omega_0^*) = \Delta x^*/2\pi \sum_{n=0}^{N-1} w_s(n)P_r(n\Delta x^*, \omega_0^*)e^{-ik_1^* n\Delta x^*}. \quad (11)$$

The measured wavenumber-frequency spectrum is thus

$$S_r(k_1^*, \omega_0^*) = [1/(N\Delta x^* M\Delta t^* C_1 C_2)] |H_r(k_1^*, \omega_0^*)|^2, \quad (12)$$

where C_1 and C_2 are corrections for the temporal and spatial windows given by

$$\begin{aligned} C_1 &= (1/M) \sum_{j=0}^{M-1} w_t^2(j), \\ C_2 &= (1/N) \sum_{j=0}^{N-1} w_s^2(j). \end{aligned} \quad (13)$$

We choose the Hanning window given by $w(q) = 1 - \cos^2[\pi q/(Q - 1)]$, $q = 0, 1, 2, \dots, Q-1$, with side lobes 32 dB below the main lobe, for both the temporal and spatial cases. The ensemble averaged wavenumber-frequency spectrum is then

$$S(k_1^*, \omega_0^*) = 1/R \sum_{r=1}^R S_r(k_1^*, \omega_0^*). \quad (14)$$

Equations (10) through (14) may be used directly to determine $S(k_1^*, \omega_0^*)$. However, existing fast Fourier transform (FFT) routines are preferable so as to compute the discrete Fourier transforms more efficiently. A block diagram showing the sequence of steps in the computation of $S(k_1^*, \omega_0^*)$ is shown in figure 4.

We now consider the errors that result from the spatial response of the sensors and also from the wavenumber filter. We note that filtering in the spatial domain is analogous to filtering in the time domain. However, aliasing in the spatial domain is more difficult to eliminate, as will be shown. The relationship between the measured and the true spectrum is given by

$$S(k_1^*, \omega_0^*) = \int_{-\infty}^{\infty} \int_{-\infty}^{\infty} E(k_1^*, k_2^*, \omega_0^*) |Q^*(k_1^*, k_2^*)|^2 (1/N\Delta x^* 2\pi C_2) |Z^*(k_1^* - k_1^*)|^2 dk_1^* dk_2^*, \quad (15)$$

where the normalized sensor response is given by

$$Q^*(k_1^*, k_2^*) = [\sin(k_1^* L_1^*/2)/(k_1^* L_1^*/2)][\sin(k_2^* L_2^*/2)/(k_2^* L_2^*/2)], \quad (16)$$

and the wavenumber filter response is

$$Z^*(k_1^*) = \Delta x^* \sum_{q=0}^{N-1} w_s(q) e^{-ik_1^* q \Delta x^*}. \quad (17)$$

We first consider errors resulting from the sensor response $Q^*(k_1^*, k_2^*)$. The Corcos model for $E^*(k_1^*, k_2^*, \omega_0^*)$ given by equation (7) and the sensor response $Q^*(k_1^*, k_2^*)$ given by equation (16) are both separable in k_1^* and k_2^* . We define

$$E^*(k_1^*, k_2^*, \omega_0^*) |Q^*(k_1^*, k_2^*)|^2 = g_1^*(k_1^*, L_1^*) g_2^*(k_2^*, L_2^*), \quad (18)$$

where

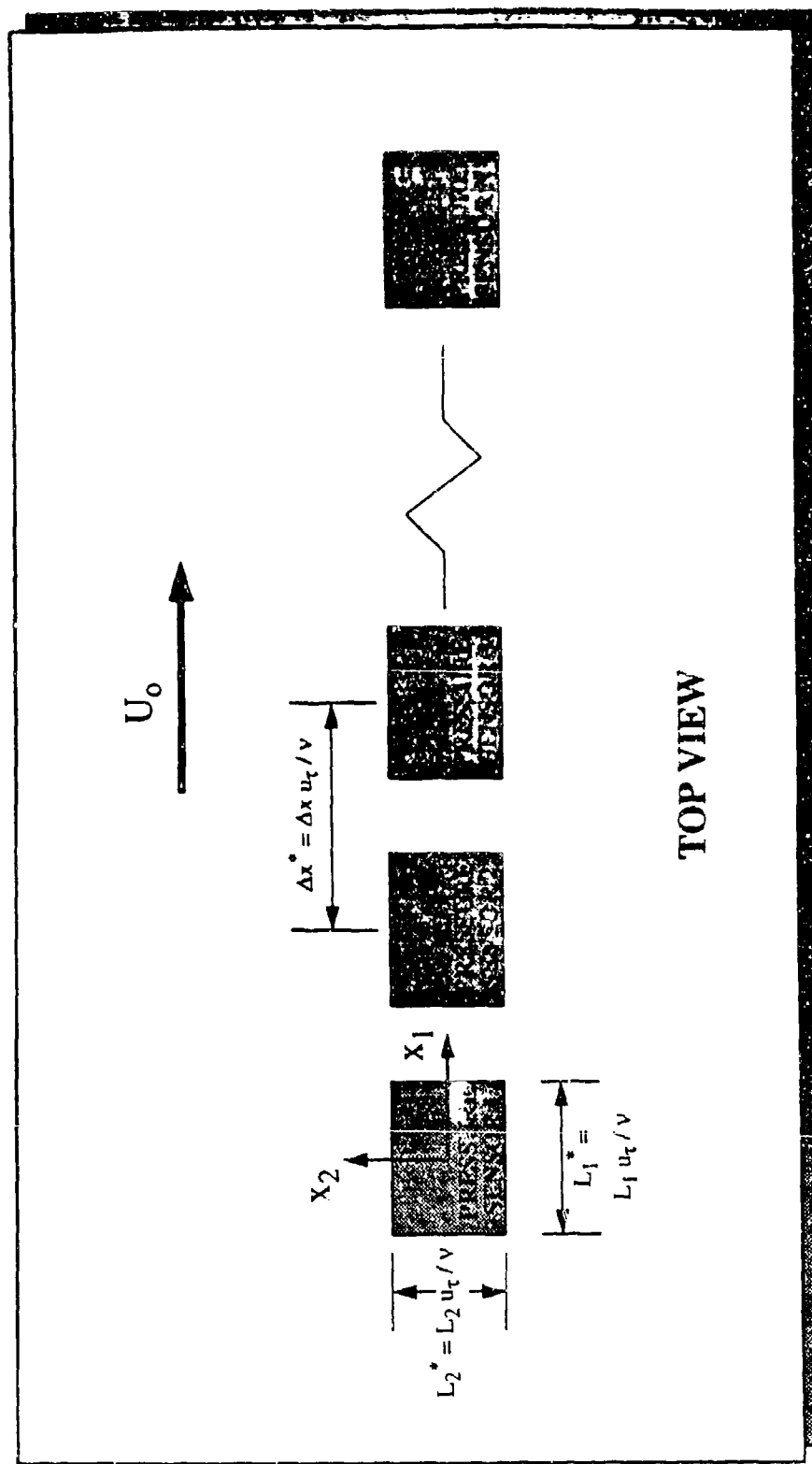


Figure 3. Wavenumber Filter Details

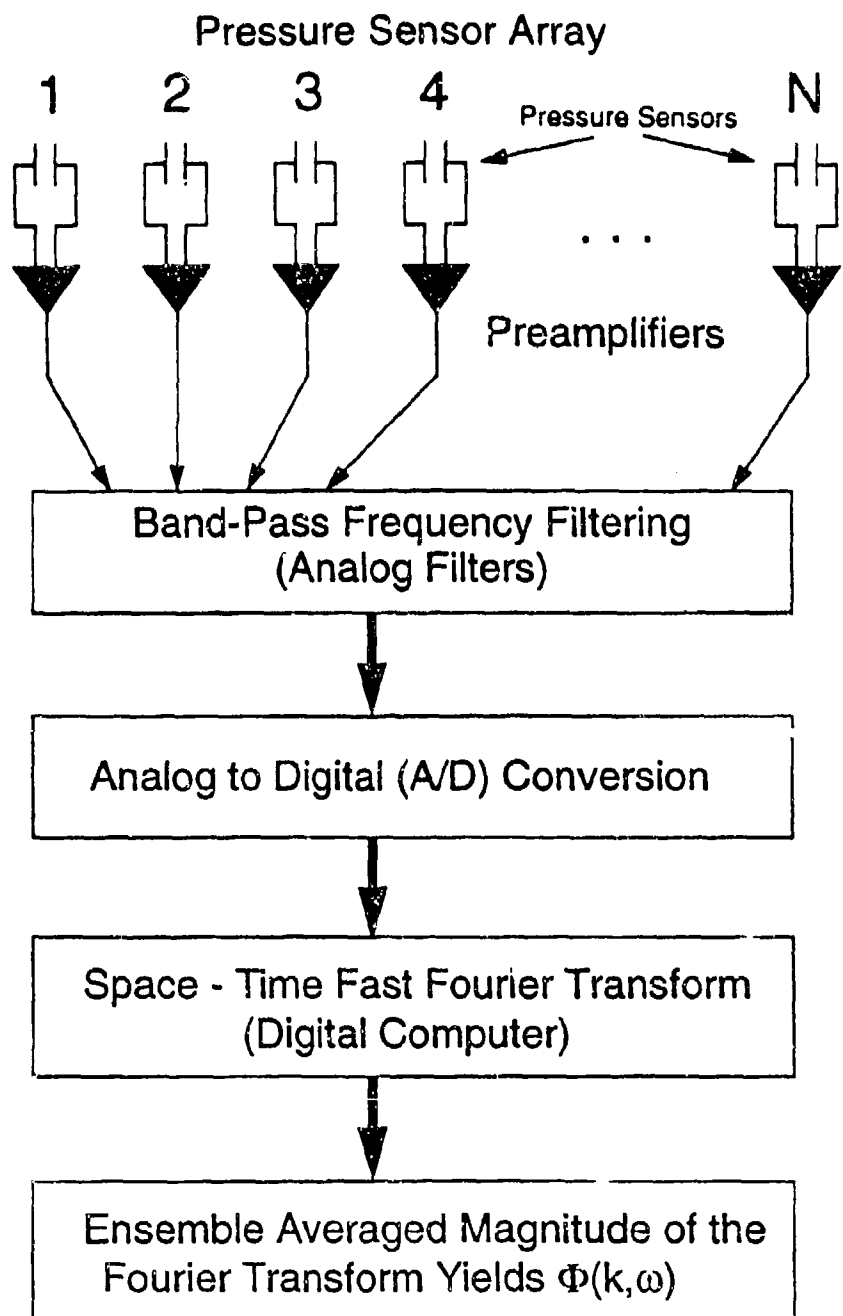


Figure 4. Signal Processing Flow Chart

$$g_1^*(\kappa_1^*, L_1^*) = F_1^*(\kappa_1^*) [\sin(\kappa_1^* L_1^*/2)/(\kappa_1^* L_1^*/2)]^2, \quad (19)$$

$$g_2^*(\kappa_2^*, L_2^*) = F_2^*(\kappa_2^*) [\sin(\kappa_2^* L_2^*/2)/(\kappa_2^* L_2^*/2)]^2,$$

and $F_1^*(\kappa_1^*)$ and $F_2^*(\kappa_2^*)$ are given by equation (8). From equation (15), the effect of the spanwise dimension L_2^* on $S(k_1^*, \omega_0^*)$ is given by

$$G_2^*(L_2^*) = \int_{-\infty}^{\infty} g_2^*(\kappa_2^*, L_2^*) d\kappa_2^*. \quad (20)$$

For a particular L_2^* , the measured spectrum $S(k_1^*, \omega_0^*)$ is reduced by a constant amount at all k_1^* and ω_0^* . Equation (20) was evaluated using MACSYMA to obtain

$$G_2^*(L_2^*) = 2[e^{(\beta k_c^* L_2^*)} - \beta k_c^* L_2^* - 1]/(\beta k_c^* L_2^*)^2. \quad (21)$$

The function $G_2^*(L_2^*)$ is shown in figure 5. For $L_2^* = 2$, a 10-percent (0.5 dB) reduction in the level of $S(k_1^*, \omega_0^*)$ occurs, and for $L_2^* = 5$, a 20-percent (1 dB) reduction occurs. Further insight into the spatial response of the sensor may be gained by examining the function $g_2^*(\kappa_2^*, L_2^*)$. This function is shown in figure 6 for $L_2^* = 0$ (true spectrum), 5, 10, 20, and 100. Here, both the main lobe of the spanwise sensor response and the dominant energy in the true spectrum are centered around $\kappa_2^* = 0$. The spatial filtering of the sensor is significant at higher positive and negative wavenumbers due to the broad energy content of the true spectrum. The wavenumber range $-1 < \kappa_2^* < 1$ of figure 6 contains approximately 90 percent of the energy existing in the true spectrum over all wavenumbers. For values of L_2^* greater than 5, the sensor filtering dominates, as evident from the side lobe patterns in the figure. We choose $L_2^* = 5$ as an acceptable design parameter, but note that smaller sensors are desirable.

An acceptable size for L_1^* can only be determined by considering the sensor response in conjunction with the wavenumber filter response, as evident from equation (15). The filtering of high wavenumbers by the sensor limits the energy that is aliased into the wavenumber range of interest. We first compare the effect of the sensor response alone on the true spectrum, as this determines the field that the wavenumber filter operates on. Since we are measuring $S(k_1^*, \omega_0^*)$, the function $g_1^*(\kappa_1^*, L_1^*)$ itself determines the filtering effect of the sensor. This function is shown in figure 7, for $L_1^* = 0$ (true spectrum), 5, 10, 20, and 100. The main lobe of the sensor response is again centered around $\kappa_1^* = 0$, but the dominant energy in the true spectrum is centered

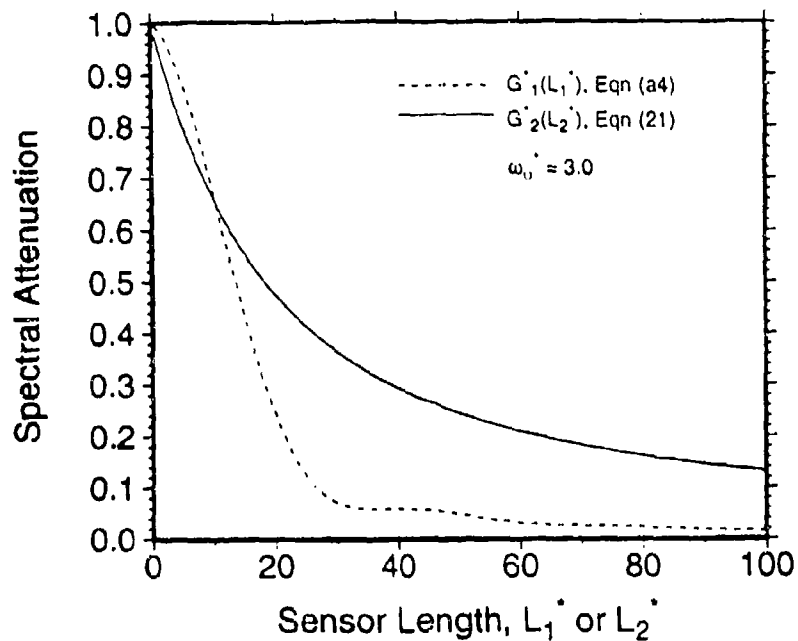


Figure 5. Spectral Attenuation the High Frequency Due to the Spanwise or Streamwise Sensor Length

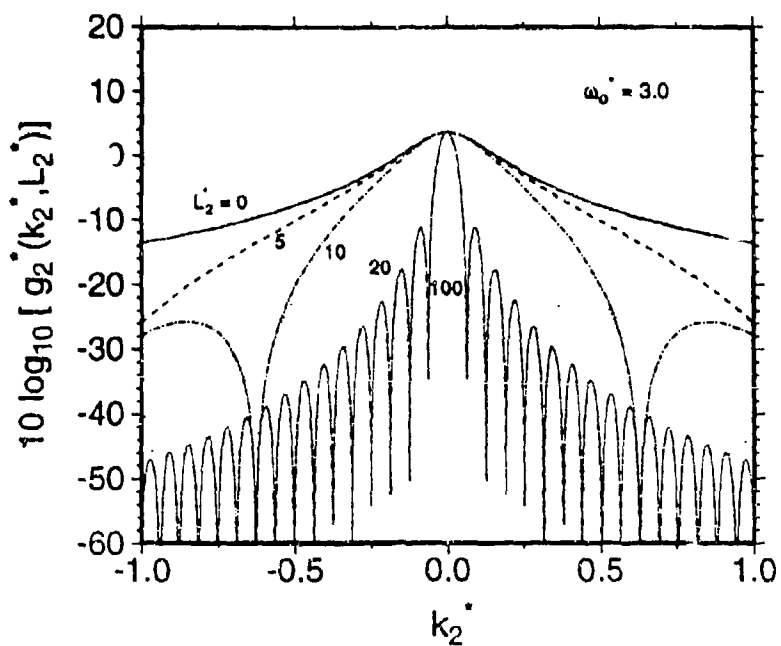


Figure 6. The Product of the Spanwise Sensor Response (for $0 \leq L_2^* \leq 100$) and the True Spectrum for the High-Frequency Case

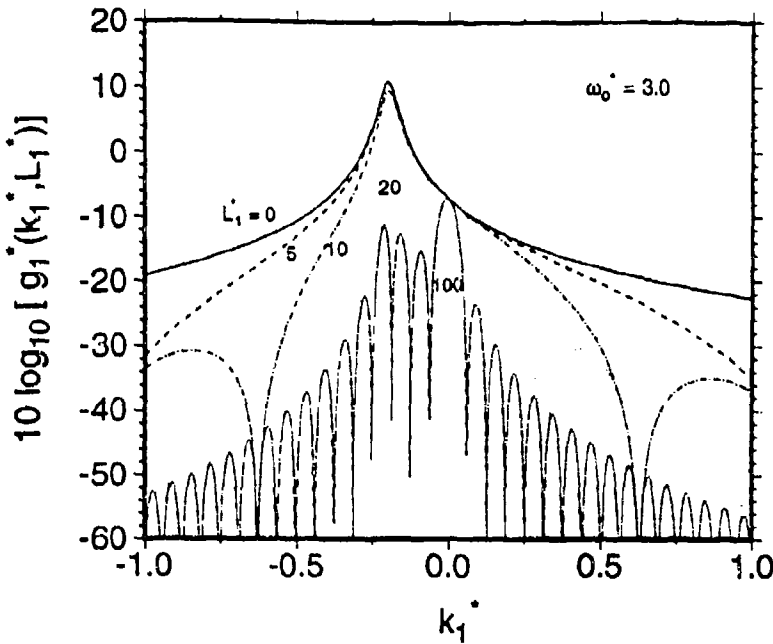


Figure 7. The Product of the Streamwise Sensor Response (for $0 \leq L_1^* \leq 100$) and the True Spectrum for the High-Frequency Case

around $\kappa_1^* = -0.2$. For $L_1^* = 5$, the peak in $g_1^*(\kappa_1^*, L_1^*)$ occurs at $\kappa_1^* = -0.2$, and the peak level is reduced by 8 percent (or 0.4 dB). For $L_1^* = 10$, the peak is shifted by 0.5 percent toward the origin, and the peak level is reduced by 29 percent (or 1.5 dB). For larger values of L_1^* , the sensor filtering dominates the measured spectrum, as shown by the side lobe patterns. We select $L_1^* = 5$, and determine the effect of the wavenumber filter on the measured spectrum.

With $L_2^* = 5$, a 20-percent reduction was shown to occur in $S(k_1^*, \omega_0^*)$. We express equation (15) as

$$S(k_1^*, \omega_0^*) = C_3 \int_{-\infty}^{\infty} g_1^*(\kappa_1^*)(1/N\Delta x^* 2\pi C_2) |Z^*(\kappa_1^* - k_1^*)|^2 d\kappa_1^*, \quad (22)$$

where $C_3 = 0.8$. In order to determine the effect of the wavenumber filter on the measured spectrum, we consider the quantity $S(k_1^*, \omega_0^*)/C_3$ defined as $S_1(k_1^*, \omega_0^*)$ and do not include the 20-percent reduction, which is constant at all k_1^* . The filter function given by

$$V(\kappa_1^* - k_1^*) = (1/N\Delta x^* 2\pi C_2) |Z^*(\kappa_1^* - k_1^*)|^2 \quad (23)$$

is periodic in wavenumber at period $2\pi/\Delta x^*$. The number of sensors N and spacing Δx^* determine the wavenumber bin width $\Delta k^* = 2\pi/N\Delta x^*$. We initially define $\Delta x^* = 10$ (allowing for finite spacing between the sensors) and $N = 100$. The filter function $V(k_1^* - k_1^*)$ is shown in figure 8, where the main lobe is centered at $k_1 = -0.2$. In comparison, we also show the filter function for the case $\Delta x^* = 5$ and $N = 100$ with the main lobe centered at $k_1 = -0.6$ (for clarity). Decreasing the spacing from 10 to 5 viscous lengths (with the number of sensors held constant) increases the wavenumbers at which the aliasing lobes occur by a factor of two. In addition, the main lobe (and aliasing lobes) becomes slightly broader, and the wavenumber bin width increases by a factor of 2. It is therefore desirable to maximize the number of sensors to achieve a narrow main lobe and bin width. In addition, minimizing the sensor spacing causes the aliasing lobes to occur at wavenumbers where the spectral levels are low. We also utilize the filtering provided by the sensors (previously discussed) to reduce the spectral levels at which the aliasing lobes occur, since the field that the filter function operates on is effectively prefiltered by the sensors.

The measured spectrum $S_1(k_1^*, \omega_0^*)$ was computed numerically for three different cases, as shown in figure 9. The first case is for 100 infinitesimally small sensors ($L_1^* = 0$) and $\Delta x^* = 10$ in order to illustrate the effect of the filter function $V(k_1^* - k_1^*)$ alone on the measured spectrum. The measured spectrum is periodic at $2\pi/10$, and agrees well with the true spectrum in the convective ridge region for $-0.31 < k_1^* < -0.09$. For $k_1^* > -0.09$, the measured levels are higher than the true levels due to aliasing. The second case is for 100 sensors with $L_1^* = 5$ and $\Delta x^* = 10$. The measured levels are slightly lower than the true levels for $k_1^* < -0.2$ due to the filtering from the sensors (note the measured levels for case 2 and case 3 are identical over this wavenumber range). For $-0.2 < k_1^* < 0$, the measured levels agree well with the true levels, with the aliased energy reduced due to the sensor filtering. For $0 < k_1^*$, aliased energy is apparent. The third case involves 200 sensors with $L_1^* = 5$ and $\Delta x^* = 5$. The measured levels agree well with the second case for $k_1^* < 0$. For $0 < k_1^*$ the measured levels agree very well with the true spectrum. The aliased energy apparent for cases 1 and 2 over this wavenumber range is reduced. This is due to the smaller sensor spacing, which places the aliasing lobes farther from the main lobe. Here, the smaller spacing leads to increased accuracy at low values of $|k_1^*|$. We select the parameters for the second case, which result in a good estimate of the true spectrum around the convective ridge and allow for finite spacing between the sensors, which is desirable for fabricating the array of sensors.

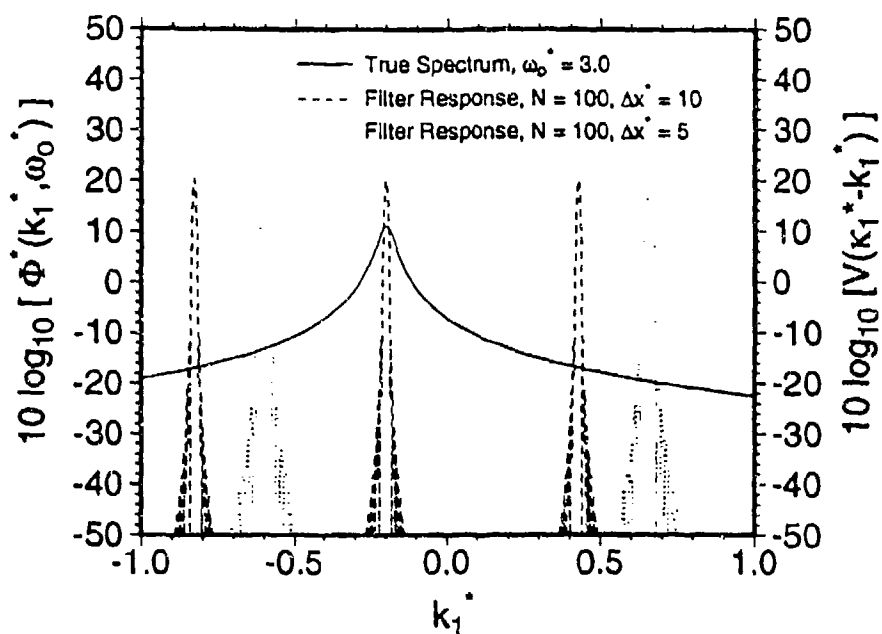
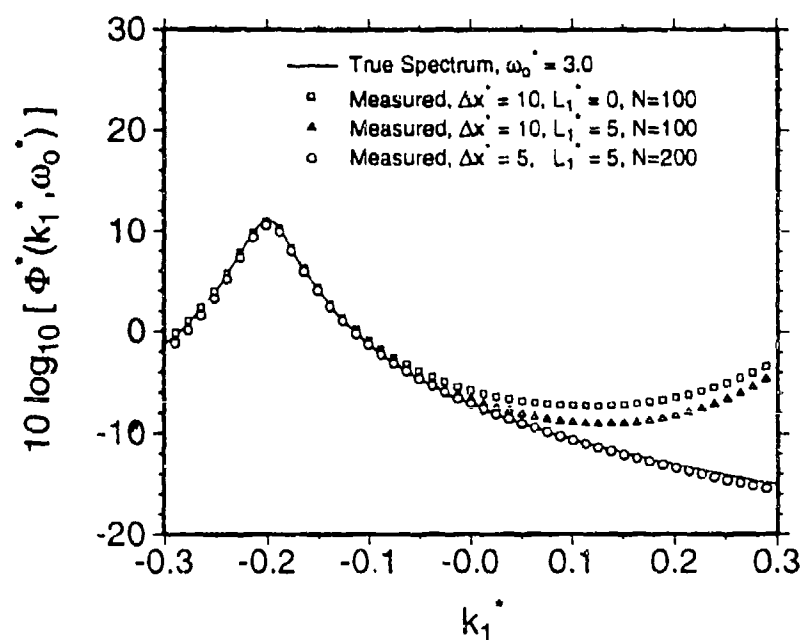


Figure 8. The Wavenumber Filter Responses Compared With the True Spectrum for the High-Frequency Case



DATA POINTS ARE DISPLAYED AT EVERY SECOND WAVENUMBER BIN FOR CLARITY

Figure 9. Comparison of the Measured Spectrum (for Three Different Wavenumber Filters) With the True Spectrum at the High Frequency

MEASUREMENTS AT LOW FREQUENCIES

We now consider the measurement of the wavenumber frequency spectrum at low frequencies. The lowest frequency at which measurements may be made is often determined by the background acoustic noise in the experimental facility. The use of noise cancellation techniques as discussed by Farabee and Casarella (1991) can allow measurements to be made at frequencies where acoustic noise exists. However, an absolute low-frequency limit valid for any boundary layer cannot be specified. With regard to the turbulence physics, it is desirable to make measurements at as low a frequency as is physically possible for a particular facility or test. Here we arbitrarily choose a low frequency and determine suitable parameters for the measurement of the wavenumber frequency spectrum.

Farabee and Casarella (1991) defined a frequency region $5 \leq \omega\delta/u_\tau \leq 100$, where the dominant sources for $\Phi(\omega)$ are from velocity fluctuations in the outer region of the turbulent boundary layer. We choose $\omega_0\delta/u_\tau = 20$ which falls within this range. The relationship between the outer and inner frequency scaling is given by $\omega_0^* R_\tau = \omega_0\delta/u_\tau$, where $R_\tau = \delta u_\tau/v$. With $R_\tau = 2010$ (for the highest Reynolds number of Farabee and Casarella (1991)), $\omega_0^* = .01$. The value for the streamwise decay constant α was taken as -0.24, from the results of Farabee and Casarella (1991) at the lower frequencies. The spanwise decay constant β was taken as -0.7, from the results of Willmarth and Roos (1965). For convenience, we will retain the inner variable scaling for displaying the spectra, but note an outer variable scaling is appropriate at low frequencies, as discussed by Farabee and Casarella (1991) and Keith et al. (1992).

For measurements at low frequency, sensor size requirements are significantly less restrictive than for those at high frequency. This is due to the more narrow distribution of energy in both k_1^* and k_2^* in the true spectrum at low frequencies, as shown in figures 2 and 10. Larger values of L_1^* are in fact desirable for reducing aliased energy, as previously discussed. The reduction in spectral levels due to the spanwise length is negligible (within 2 percent) for $L_2^* \leq 100$, as shown by the values for $G_2^*(L_2^*)$ in figure 11. We define $L_2^* = 100$, but note that larger values are acceptable.

A smaller wavenumber bin width is required to resolve the narrower distribution of energy around the convective ridge. The overall length of the wavenumber filter must therefore be increased. We define the bandwidth Δk over which the spectrum levels are within 3 dB of the peak level at the convective ridge. For the high-frequency case, Δk contains eight wavenumber bins. We choose 100 sensors with length $L_1^* = 100$ and spacing $\Delta x^* = 1480$, which yields eight

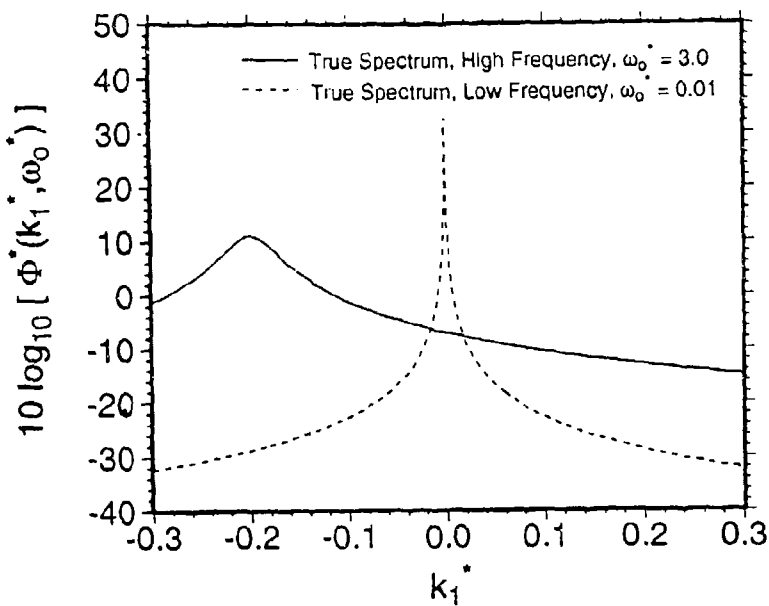


Figure 10. Nondimensional Wavenumber-Frequency Spectrum for the High- and Low-Frequency Cases From the Corcos Model

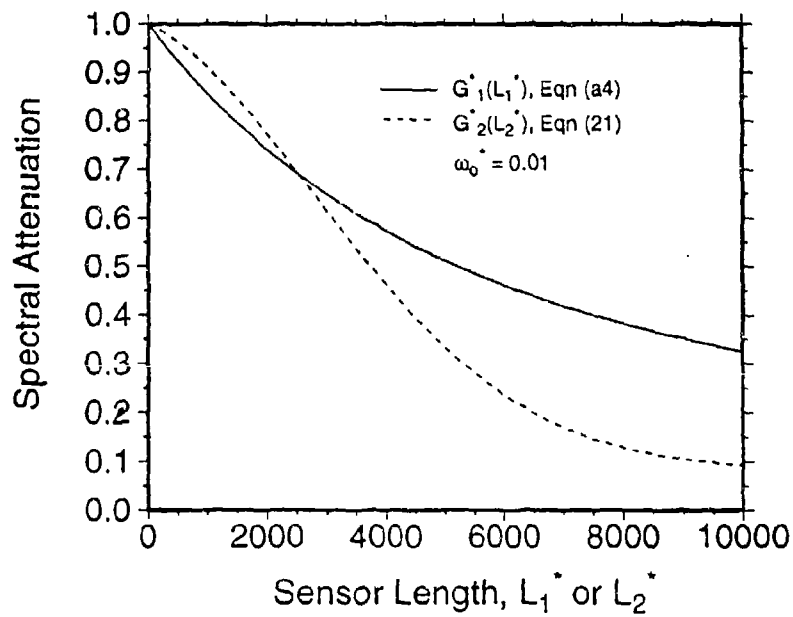


Figure 11. Spectral Attenuation at the Low Frequency Due to the Spanwise or Streamwise Sensor Length

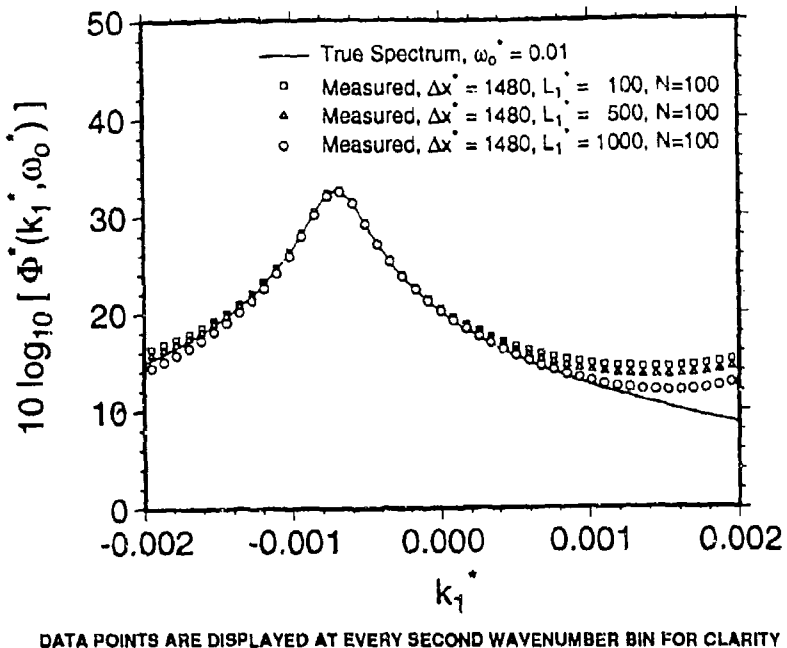


Figure 12. Comparison of the Measured Spectrum (for Three Different Wavenumber Filters) With the True Spectrum at the Low Frequency

bins over Δk for the low-frequency case. The measured spectrum for this case is shown in figure 12. The convective ridge region is accurately resolved, and the increased levels at higher and lower wavenumbers occur from aliasing. The overall length of the wavenumber filter for this case is 148,000 viscous lengths. Also shown in figure 12 are the cases for $L_1^* = 500$ and $L_1^* = 1000$, with the same number of sensors and sensor spacing. Increasing the sensor length increases the wavenumber range over which the convective ridge region is accurately resolved, due to the filtering of wavenumbers that are aliased. For the $L_1^* = 1000$ case, the spectral levels are below the true levels at the higher negative wavenumbers, but agree well at the higher positive wavenumbers. The $L_1^* = 500$ length is chosen for the purpose of designing a filter at this low frequency.

Clearly, separate wavenumber filters are required at high and low frequencies. To achieve an overall filter length of 148,000, required for the low-frequency case (as shown), the number of sensors needed using a 10 viscous length spacing (corresponding to the high-frequency filter) is 14,800. This is impractical in view of the signal processing requirements as well as the wavenumber filter fabrication. For a particular application, we may need to design a number of filters to cover the frequency ranges of interest. The dynamic range required for individual sensors therefore depends on the frequency range of the wavenumber filter for which they will be used.

DIMENSIONAL WAVENUMBER FILTER PARAMETERS FOR TURBULENT BOUNDARY LAYERS IN AIR AND WATER

We consider boundary layers from particular wind tunnel and water tunnel investigations, and also an external boundary layer that could exist in an undersea application, such as flow over a hull. The boundary layer parameters and the proposed wavenumber filter parameters for the high frequency case are given in table 1. Regarding the two wind tunnel investigations, Willmarth and Wooldridge (1962) worked at a high free-stream velocity, but their thicker boundary layer led to a viscous length scale comparable to that of Farabee and Casarella (1991). For the investigation using water, the boundary layer thicknesses were comparable, but the higher free-stream velocity of Carey et al. (1967) led to a smaller viscous length scale than that of Keith and Barclay (1986). For the undersea application, the boundary layer parameters were obtained from Cope (1975) for ideal smooth wall, zero pressure gradient, flat plate case. The location from the turbulent boundary layer origin was taken as approximately 100 ft. The viscous length scale is comparable to the other water flows, and the boundary layer is thicker.

The required sensor sizes for these cases are on the order of 10 microns. The required length $N\Delta x$ of the wavenumber filter (based upon 100 sensors at 10 viscous length spacing) varies from the order of 0.1 to 1.0 cm. The d^4 values actually used in each investigation are also given. The small viscous length scales for the water flows led to large d^4 values. For the water tunnel investigation of Keith and Barclay, the actual sensor diameter was 0.2 mm, which corresponded to 444 viscous lengths. The required sensor sizes, as well as the sensor spacings, for these cases emphasize the requirement for microfabrication technology for such applications, particularly in water.

CONCLUSIONS AND RECOMMENDATIONS

The analysis presented here shows that the measurement of turbulent wall pressure wavenumber-frequency spectra at high frequencies for Rg values of practical interest in air or water requires microfabrication technology. The spanwise, as well as the streamwise, sensor length is significant in reducing the measured spectral levels. For the measurement of the wavenumber-frequency spectrum $\Phi(k_1, \omega)$, the streamwise sensor length also limits the sensor spacing and affects the amount of aliased energy.

We have considered two particular frequencies requiring two wavenumber filter designs. At high frequencies, a short overall filter length and small sensor size and sensor spacing are required

At low frequencies, the filter length is two orders of magnitude greater, as is the sensor spacing. In addition, sensors that are two orders of magnitude greater in streamwise length are required to reduce vorticity energy.

We have assumed ideal rectangular sensors with known wavenumber-frequency responses. In practice, even though the frequency response of sensors can be measured, the wavenumber-frequency response is unknown and not easily measured. While rectangular sensors may be preferable for manufacturing with microfabrication technology, our analysis can also be extended to circular sensors. We have used the Corcos model here, but other models may be considered. Neither the uncertainties due to the sensor responses nor the selected model will significantly affect the conclusions presented in this paper.

At the present time, the accurate measurement of ensemble averaged wavenumber-frequency spectra of equilibrium boundary layer wall pressure fluctuations is of significant interest because of the lack of published data. However, the interpretation of such measurements in relation to the physics of the turbulent boundary layer will require conditional sampling as well as parametric studies. The effect of R_0 on the measured spectrum will be of particular interest, especially for comparison with results from numerical simulations that are constrained to lower R_0 values. In addition, the measured spectra from perturbed or nonequilibrium boundary layers will also provide additional physical insight. It is hoped that microfabrication technology will allow such measurements to be pursued in the future.

REFERENCES

- Blake, W. K., and D. M. Chase (1971), "Wavenumber-Frequency Spectra of Turbulent-Boundary-Layer Pressure Measured by Microphone Arrays," *Journal of the Acoustical Society of America*, vol. 49, no. 3 (pt. 2), pp. 862-877.
- Carey, G. F., J. E. Chlupsa, and H. H. Schloemer (1967), "Acoustic Turbulent Water-Flow Tunnel," *Journal of the Acoustical Society America*, vol. 41, no. 2, pp. 373-379.
- Choi, H., and P. Moin (1990), "On the Space-Time Characteristics of Wall-Pressure Fluctuations," *Physics of Fluids* (A), 2 (8), August, pp. 1450-1460.
- Coles, D. (1953), "Measurements in the Boundary Layer on a Smooth Flat Plate in Supersonic Flow, Pt.1, The Problem of the Turbulent Boundary Layer," Report No. 20-69, Jet Propulsion Laboratory, California Institute of Technology, Pasadena, CA.
- Corcos, G. M. (1963), "Resolution of Pressure in Turbulence," *Journal of the Acoustical Society of America*, vol. 35, no. 2, February, pp. 192-199.
- Farabee, T. M., and F. E. Geib (1991), "Measurements of Boundary Layer Pressure Fluctuations at Low Wavenumbers on Smooth and Rough Walls," *Proceedings of the ASME Symposium on Flow Noise Modeling, Measurement, and Control*, NCA vol. 11/FED vol. 130, Atlanta, December 1-6.
- Farabee, T. M., and M. J. Casarella (1991), "Spectral Features of Wall Pressure Fluctuations Beneath Turbulent Boundary Layers," *Physics of Fluids A*, 3 (10), October, pp. 2410-2420.
- Head, M. R., and P. Bandyopadhyay (1981), "New Aspects of Turbulent Boundary Layer Structure," *Journal of Fluid Mechanics*, vol. 107, pp. 297-338.
- Karangelon, C. C., M. J. Casarella, and T. M. Farabee (1991), "Wavenumber-Frequency Spectra of Turbulent Wall Pressure Fluctuations," *Proceedings of the ASME Symposium on Flow Noise Modeling, Measurement, and Control*, NCA vol. 11/FED vol. 130, Atlanta, December 1-6.
- Keith, W. L., and J. J. Barclay (1993), "Effects of a Large Eddy Breakup Device on the Fluctuating Wall Pressure Field," *Journal of Fluids Engineering*, vol. 115, no. 3, September, pp. 389-397.
- Keith, W. L., D. A. Hurdis, and B. M. Abraham (1992), "A Comparison of Turbulent Boundary Layer Wall Pressure Spectra," *Journal of Fluids Engineering*, vol. 114, no. 3, September, pp. 338-347.
- Manoha, E. (1991), "Wall Pressure Wavenumber-Frequency Spectrum Beneath a Turbulent Boundary Layer Measured With Transducer Arrays Calibrated With an Acoustical Method," *Proceedings of the ASME Symposium on Flow Noise Modeling, Measurement, and Control*, NCA vol. 11/FED vol. 130, Atlanta, December 1-6.
- Rand, R. H. (1984), *Computer Algebra in Applied Mathematics: An Introduction to MACSYMA*, Pitman, MA.

- Schewe, G. S. (1983), "On the Structure and Resolution of Wall-Pressure Fluctuations Associated With Turbulent Boundary Layers," *Journal of Fluid Mechanics*, vol. 134, pp. 311-328.
- Smol'yakov, A. V., and V. M. Tkachenko (1983), *The Measurement of Turbulent Fluctuations*, Springer-Verlag, New York, pp. 178-190.
- Wei, T., and W. W. Willmarth (1989), "Reynolds-Number Effects on the Structure of a Turbulent Channel Flow," *Journal of Fluid Mechanics*, vol. 204, pp. 57-95.
- Willmarth, W. W., and F. W. Roos (1965), "Resolution and Structure of the Wall Pressure Field Beneath a Turbulent Boundary Layer," *Journal of Fluid Mechanics*, vol. 22, no. 1, pp. 81-94.
- Willmarth, W. W., and C. E. Wooldridge (1962), "Measurements of the Fluctuating Pressure at the Wall Beneath a Thick Turbulent Boundary Layer," *Journal of Fluid Mechanics*, vol. 14, no. 2, pp. 187-210.

APPENDIX

SENSOR SIZE EFFECTS ON MEASURED FREQUENCY SPECTRA

Although we have focused on the measurement of the wavenumber-frequency spectrum, microfabrication technology is important for single-point measurements of the frequency spectrum $\Phi_m(\omega_0)$. For our case, the relationship between the measured and true (one dimensional) frequency spectrum may be expressed as

$$\Phi_m(\omega_0) = \Phi_t(\omega_0) \int_{-\infty}^{\infty} \int_{-\infty}^{\infty} g_1^*(\kappa_1^*, L_1^*) g_2^*(\kappa_2^*, L_2^*) d\kappa_1^* d\kappa_2^*, \quad (A-1)$$

which reduces to

$$\Phi_m(\omega_0) = \Phi_t(\omega_0) G_1^*(L_1^*) G_2^*(L_2^*), \quad (A-2)$$

where $G_2^*(L_2^*)$ is given by equation (21) and

$$G_1^*(L_1^*) = \int_{-\infty}^{\infty} g_1^*(\kappa_1^*, L_1^*) d\kappa_1^*. \quad (A-3)$$

Equation (A-3) was evaluated using MACSYMA to obtain

$$G_1^*(L_1^*) = 2[e(\alpha k_c^* L_1^*) (2\alpha \sin(k_c^* L_1^*) + (\alpha^2 - 1) \cos(k_c^* L_1^*)) \\ - \alpha(\alpha^2 + 1) k_c^* L_1^* - \alpha^2 + 1]/[(\alpha^4 + 2\alpha^2 + 1) k_c^* L_1^{*2}]. \quad (A-4)$$

The functions $G_1^*(L_1^*)$ and $G_2^*(L_2^*)$ are shown in figure 5 for the high-frequency case. From equations (21) and (A-4),

$$\left. \frac{dG_2^*}{dL_2^*} \right|_{L_2^* = 0} = 5 \left. \frac{dG_1^*}{dL_1^*} \right|_{L_1^* = 0}. \quad (A-5)$$

For small values of L_1^* and L_2^* , the spanwise sensor length therefore causes a greater reduction in spectral level than the same streamwise length. For $L_1^* = L_2^* = 10.4$, the spanwise and

streamwise effects are comparable. For larger values of L_1^* and L_2^* , the streamwise length dominates the reduction.

The functions $G_1^*(L_1^*)$ and $G_2^*(L_2^*)$ are shown in figure 11 for the low-frequency case. These functions are similar to the high-frequency case, with the L_2^* effect dominant for sensor lengths of less than 2500, and the L_1^* effect dominant at larger values. However, the actual values of L_1^* and L_2^* required for a particular reduction are generally two orders of magnitude greater than for the high-frequency case. This reflects the change in the energy distribution in the true spectrum at low frequencies, as shown in figures 2 and 10. The reductions are negligible for L_1^* and $L_2^* \leq 100$. For measurements at low frequency, sensor size requirements are therefore significantly less restrictive than for those at high frequency.

INITIAL DISTRIBUTION LIST

Addressee	No. of Copies
Defense Technical Information Center	12
Northwestern University, Dept. of Mechanical Engineering (Prof. R. Leuptow)	1
University of Connecticut, Dept. of Mechanical Engineering (Prof. J. Bennett, Prof. L. Langston)	2
OASIS (Dr. C. Gedney)	1
Rutgers University, Dept. of Mechanical and Aerospace Engineering (Dr. T. Wei)	1
U.S. Coast Guard Academy (Dr. V. Wilczynski, K. Colella)	2
University of Minnesota, Twin Cities Campus, Dept. of Aerospace Engineering and Mechanics (Dr. A. Alving)	1
University of Minnesota, Twin Cities Campus, Dept. of Mechanical Engineering (Prof. T. W. Simon)	1
Office of Naval Research (Dr. L. P. Purtell, Dr. E. P. Rood, Dr. K. Ng)	3
NASALRC (Dr. J. C. Hardin)	1
The Catholic University of America (Prof. M. Casarella)	1
Tufts University (Prof. V. P. Manno)	1
Naval Surface Warfare Center, Carderock Division (Dr. T. Farabee, P. Chang)	2
University of Michigan (Dr. P. B. Washabaugh)	1
TSI, Inc. (G. Reynolds)	1
General Atomics (Dr. C. R. Harder, P. W. Trester)	2